



Full length article



# Unsteady Flamelet modeling study on OME<sub>x</sub>-type fuels under Engine Combustion Network Spray A conditions

Jesus Benajes, Jose M. Garcia-Oliver<sup>\*</sup>, Jose M. Pastor, Daiana De Leon-Ceriani

CMT - Motores Térmicos, Universitat Politècnica de València, Edificio 6D, Camino de Vera s/n, Valencia 46022, Spain

## ARTICLE INFO

### Keywords:

Poly-Oxymethylene Dimethyl Ethers  
ECN  
Spray A  
CFD  
Flamelet

## ABSTRACT

Poly-Oxymethylene Dimethyl Ethers OME<sub>x</sub> are synthetic and potentially-renewable fuels that lead to a notable reduction of the lifecycle CO<sub>2</sub> emissions while promoting lower soot emissions than conventional Diesel fuel. In the present contribution, a computational study with a single component OME1 and a multicomponent OME<sub>x</sub> fuel has been carried out under reference Spray A conditions from the Engine Combustion Network (ECN), which mimic in-cylinder conditions representative of Diesel engines. For both fuels, three ambient temperature conditions have been swept at constant ambient density. Calculations have been carried out using an Unsteady Flamelet Progress Variable (UFPV) combustion model and detailed chemical mechanisms. For both OME<sub>x</sub>-type fuels, low temperature ignition in flamelet configurations start in lean mixtures, which shifts towards the fuel-rich zone and eventually leads to high temperature ignition, similar to typical hydrocarbons. In agreement with corresponding fuel cetane numbers, ignition of OME<sub>x</sub> occurs at timings similar to those of n-dodecane, which is the reference fuel for ECN studies, while a delayed ignition is obtained for OME1. However, the actual difference in ignition timing between OME<sub>x</sub> and n-dodecane depends on diffusion in the mixture fraction space. Moreover, ignition in spray calculations seems to occur fully on the lean side, especially for OME1, as well as for the low temperature cases. This difference in ignitable mixture range between the canonical flamelet configuration and the spray calculations results from the finite residence time for relevant mixtures in the latter case, compared to an infinite residence time in flamelets. Comparison with experiments show that the modeling approach predicts most combustion metrics for both fuels and temperature values. The combination of ambient temperature and fuel-related reactivity has enabled a transition from a short ignition lifted diffusion flame structure (OME<sub>x</sub> at 1000–900 K) towards long ignition cases, where lift-off length may eventually be longer than the maximum length of the stoichiometric surface. This results in a reaction front stabilization at very lean conditions, i.e. a type of lean mixing-controlled flame.

## 1. Introduction

Due to the steady increase in energy consumption and the simultaneous restrictive objectives to reduce greenhouse gas emissions it is necessary, among other environmental measures, to reduce the consumption of fossil fuels, which make up the main worldwide energy source so far. The transport sector is particularly immersed in an unstoppable and promising transition towards electric mobility, but in any case, the autonomy needs of the vehicle make electrification difficult for high power and long range applications. For this reason, the use of propulsion plants based on combustion engines in the short-medium term will continue to be necessary. This means that fossil fuels will have to be replaced, regardless of electrification, by other sustainable alternatives, mainly in the form of synthetic and renewable fuels [1,2]. This change will be achievable if the emission of pollutant emissions comply with the corresponding regulation [3,4].

Among different synthetic and renewable-based fuels currently under evaluation, the family of the so-called poly-Oxymethylene Dimethyl Ethers have turned out to be very promising candidates. Their general formula  $\text{CH}_3\text{O} - (\text{CH}_2\text{O})_n - \text{CH}_3$ , with  $n > 0$ , shows that they are oxygenated molecules that are characterized by the absence of carbon-carbon bonds. Furthermore, they have compatible physical and chemical properties for their use in conventional propulsion systems. These fuels are the focus of an important activity in the transport sector in the transition towards decarbonization [5,6]. The particular composition of this type of fuels improves the trade-off between emissions of soot and nitrogen oxides (NO<sub>x</sub>) in compression-ignition engines. This effect was studied in [7], where the increase of the OME<sub>x</sub> content in blends of diesel and gasoline was shown to reduce both soot and NO<sub>x</sub>

<sup>\*</sup> Corresponding author.

E-mail address: [jgarciao@mot.upv.es](mailto:jgarciao@mot.upv.es) (J.M. Garcia-Oliver).

<https://doi.org/10.1016/j.fuel.2022.125458>

Received 20 April 2022; Received in revised form 28 June 2022; Accepted 28 July 2022

Available online 12 September 2022

0016-2361/© 2022 The Author(s). Published by Elsevier Ltd. This is an open access article under the CC BY license (<http://creativecommons.org/licenses/by/4.0/>).

emissions. These results were also in agreement with those presented in [6].

From a more fundamental perspective, the oxygenated character of these fuels results in a different flame topology compared to that of regular hydrocarbons, as recent experimental results in a high-pressure high-temperature vessel have shown [8–10]. Using the Engine Combustion Network (ECN) single-orifice Spray A nozzle [11], the combustion process of different fuels was analyzed in [8], including  $OME_1$  and  $OME_x$ . The presence of oxygen was shown to have a major impact on the equivalence ratio at characteristic locations such as the lift-off length and flame stabilization. Furthermore, these oxygenated fuels did not produce detectable soot for the investigated conditions, in agreement with [9,12]. Additionally, laser-induced fluorescence techniques were used in [10] to resolve the spatial distribution of OH and  $CH_2O$  for  $OME_x$ . The different flame characteristics were described by means of such species and compared to n-dodecane, and the null soot production was confirmed. On the computational side, very few fundamental studies are found in the literature [5,13,14]. They all show that such fuels develop a different flame structure if compared with a reference fuel such as n-dodecane, shifting the combustion to leaner mixtures. They also confirm the reduction in soot precursor formation due to the oxygen content and its influence in the mixture fraction distribution.

The present work aims at further clarifying the differences between combustion characteristics and flame structure of  $OME_x$  and  $OME_1$  by means of computational tools. Experiments in [8–10] will be used for analysis and validation, with particular focus on the effect of the ambient temperature. The approach will start from the analysis of a canonical configuration, closed homogeneous reactors, to compare the chemical kinetics characteristics of the fuels. This will be later extended to laminar flamelets, the second canonical configuration proposed in this work, where the interaction between chemistry and diffusion will be accounted for. After that, computational fluid dynamics (CFD) calculations will be carried out for both inert and reacting configurations. For both canonical configurations, as well as for the inert spray calculations, results will be extensively compared to those of n-dodecane, which is a reference for ECN studies.

## 2. Target conditions

Following experimental work in [8–10] two fuels from the group of poly-Oxymethylene Dimethyl Ethers have been selected for the study, namely the single-component with the shortest chain  $OME_1$  and a multicomponent fuel  $OME_x$  made up of a blend of different chain lengths. The original composition of  $OME_x$  in the experimental study included 57.90%  $OME_3$ , 28.87%  $OME_4$ , 10.08%  $OME_5$ , 1.91%  $OME_6$  and negligible ( $\leq 0.01\%$ ) proportions of  $OME_1$  and  $OME_2$  (all values in weight %). As the base chemical mechanism to be used in the present study [15] only considers  $OME_2$ ,  $OME_3$  and  $OME_4$ , the original composition was simplified to 59.14%  $OME_3$  and 40.86%  $OME_4$ . n-dodecane will be used for comparison for canonical configurations (closed homogeneous reactors and flamelets) as well as inert spray calculations. Reacting spray calculations have only been performed for  $OME_x$  and  $OME_1$ , as n-dodecane has been extensively investigated in previous work [16]. The main properties of the fuels in this study are presented in Table 1.

Calculations of a single hole spray injected into an ambient at steady conditions have been performed. Operating conditions coincide with those found in [8], which were performed following ECN standards, and using Spray A injector corresponding to single-hole nozzle (reference 210675) with a diameter of 89.4  $\mu\text{m}$ , which is representative of automotive engines. Table 2 summarizes the calculated CFD cases under reacting conditions. For each fuel, three calculation cases were carried out to assess the effect of varying ambient temperature of the combustion chamber into which the fuel is injected, while keeping constant density and oxygen content.

**Table 1**  
Fuel properties [8].

Characteristic [unit]	n-dodecane	$OME_1$	$OME_x$
Density [ $\text{kg}/\text{m}^3$ ] (T = 15 °C)	751.2	866.7	1057.1
Viscosity [ $\text{mm}^2/\text{s}$ ] (T = 40 °C)	1.44	0.36	1.08
Cetane number [–]	74	28	68.6
Lubricity [ $\mu\text{m}$ ]	563	747	320
Flash point [°C]	83	<40	65
Lower heating value [MJ/kg]	44.20	19.25	19.21
Initial boiling point [°C]	214	37.40	144.90
Final boiling point [°C]	218	38	242.4
Carbon content [% m/m]	84	48.4	44.2
Hydrogen content [% m/m]	16	10.4	8.8
Oxygen content [% m/m]	0	42.1	45

**Table 2**  
Thermodynamic and fuel injection conditions for the simulated reacting CFD cases, nominal temperature in bold.

Fuel	$OME_x$ $OME_1$
Ambient Temperature	1000 K <b>900 K</b> 800 K
Ambient density	22.8 $\text{kg}/\text{m}^3$
Ambient $O_2$ composition	15%
Injection pressure	150 MPa
Fuel temperature	363 K
Nozzle diameter	89.4 $\mu\text{m}$

## 3. Modeling approach

The computational methodology in this work evaluates the fuel starting from fundamental chemistry characteristics up to turbulent spray calculations. To begin the study, canonical configurations relevant for the study, namely closed homogeneous reactors and laminar flamelets, are investigated using corresponding solvers [17,18]. As for CFD turbulent spray cases, Converge software is used [19], where the turbulence–chemistry interaction is modeled using an Unsteady Flamelet Progress Variable (UFPV) approach. Throughout all such steps, the detailed chemical mechanism by Jacobs et al. with 530 species and 2889 reactions [20] has been used for  $OME_1$ , and the mechanism developed by Cai [15] with 322 species and 1611 reactions has been used for  $OME_x$ . Whenever n-dodecane is used as a comparison, the corresponding mechanism has been the one by Yao et al. [21] with 54 species and 269 reactions.

### 3.1. Closed homogeneous reactors and laminar flamelets

In a first 0D analysis, the three fuels were investigated with homogeneous constant pressure adiabatic reactor simulations performed with Cantera [17]. Initial conditions are obtained from the adiabatic mixing between fuel and air streams in a range of equivalence ratios spanning both lean and rich conditions, similarly to the initial conditions for flamelet calculations.

Under the conditions mentioned above, the time evolution of the chemical state has been tracked following a characteristic progress variable ( $Y_c$ ). In the present study,  $Y_c$  includes the evolution of three major species ( $CO_2$ ,  $H_2O$  and  $CO$ ) according to the definition  $Y_c = 0.75Y_{CO} + Y_{CO_2} + Y_{H_2O}$ , which has been previously used in [16]. Homogeneous reactor calculations show that the relative trends among fuels do not change much with other progress variable definitions.

$$C = \frac{Y_c - Y_c^{inert}}{Y_c^{steady} - Y_c^{inert}} \quad (1)$$

A normalized version of the progress variable ( $C$ ) is used to define the ignition delay according to Eq. (1), where  $Y_c^{inert}$  and  $Y_c^{steady}$  are the inert and steady values for the progress variable, then  $0 \leq C \leq 1$ . The

ignition delay corresponding to the low- and high-temperature regions ( $ID_{HT}$ ,  $ID_{LT}$ ) are distinguished according to values of  $C = 0.1$  and  $C = 0.9$ , respectively.

In a second step, 1D laminar flamelet calculations are performed using the ZLFLAM code [18]. Flamelets in counterflow configuration are solved in mixture fraction for any ‘k’ species in the chemical mechanism space by Eq. (2).

$$\frac{\delta Y_k}{\delta t} = \frac{\chi}{2} \frac{\delta^2 Y_k}{\delta Z^2} + \dot{\omega}_k \quad (2)$$

where the chemical source term  $\dot{\omega}_k$  is obtained from the chemical mechanism. The scalar dissipation rate  $\chi$ , which considers the flamelet diffusion in mixture fraction space, is assumed to follow a steady profile following Eq. (3), as derived by Peters [22].

$$\chi(SR, Z) = \frac{SR}{\pi} \exp[-2(\text{erfc}^{-1}(2Z))^2] \quad (3)$$

In Eq. (3),  $SR$  is the strain rate, defined by the velocity gradient at the oxidizer side of the counterflow flamelet. It is possible to write the profile of  $\chi$  independent of  $SR$  by normalizing the expression with the scalar dissipation rate at stoichiometric condition  $\chi_{st}$  according to Eq. (4):

$$\chi(\chi_{st}, Z) = \chi_{st} \frac{F(Z)}{F(Z_{st})} \quad (4)$$

### 3.2. Spray combustion modeling

Spray calculations in the present work are carried out with the same computational framework as previously developed by the authors [16] for n-dodecane with the Converge code [19], so only an overall summary is provided here. The domain is a cylinder 102 mm in length and 50 mm in radius. The base mesh grid is composed of 2 mm cubes, which is generated automatically by Converge cut-cell Cartesian method. Near the nozzle area, grid mesh resolution is added using a truncated cone-shaped fixed embedding. The adaptive mesh refinement capabilities of Converge, which allow for grid refinements based upon velocity, temperature and fuel mass fraction gradients [19], have been used, so that a minimum cell size of 125  $\mu\text{m}$  is reached.

For the description of the liquid phase the Lagrangian parcel Eulerian fluid approach has been used. The Favre-averaged Navier–Stokes equations are solved within a RANS framework. The standard k- $\epsilon$  turbulence model with  $C_{\epsilon 1} = 1.55$  in order to account for round jet correction, has been used.

In terms of turbulence–chemistry interaction, an Unsteady Flamelet Progress Variable approach (UFPV) based on the concept of flamelet has been adapted and used. This approach is based upon the description of a turbulent flame as a set of strained laminar counterflow flamelets. The general workflow (Fig. 1) starts with an external tabulation of a laminar flamelet table or manifold which is done offline. The temporal evolution of the chemical reactions is represented by the progress variable  $Y_C$ , with the same definition as shown above for both closed homogeneous reactors and flamelets. The time evolution in the flamelet is re-parametrized from a temporal basis to a normalized progress variable basis (Eq. (1)).

After laminar flamelets have been calculated, the influence of turbulence is accounted for to produce a turbulent manifold, i.e. a set of tables or manifold that are used interactively during the CFD calculation. The turbulence–chemistry interaction is taken into account by considering that the mixture fraction and the scalar dissipation rate are statistical independent, using a presumed probability density function (PDF) approach for these two variables. On the one hand, a  $\beta$ -PDF function is used for the mixture fraction, which is defined by the mean value of mixture fraction ( $\tilde{Z}$ ) and the corresponding variance  $\tilde{Z}^{\prime 2}$ . This implies that a function  $P_Z(Z, \tilde{Z}, S)$  exists, with the segregation factor  $S$ , which normalizes the mixture fraction variance according to the Eq. (5).

$$S = \frac{\tilde{Z}^{\prime 2}}{\tilde{Z}(1 - \tilde{Z})} \quad (5)$$

On the other hand, a log-normal function with  $\sigma = \sqrt{2}$  is used for the scalar dissipation rate, according to  $P_\chi = (\chi_{st}, \tilde{\chi}_{st}, \sigma)$ . This means that the mean value of the scalar dissipation rate  $\tilde{\chi}$  can be obtained by the expression presented in Eq. (6).

$$\begin{aligned} \tilde{\chi} &= \left( \int_0^\infty \chi_{st} P_\chi(\chi_{st}; \tilde{\chi}_{st}, \sigma) d\chi_{st} \right) \left( \frac{1}{F(Z_{st})} \int_0^Z F(Z) P_Z(Z; \tilde{Z}, S) \right) \\ &= \tilde{\chi}_{st} J(\tilde{Z}, S) \end{aligned} \quad (6)$$

where  $J$  relates  $\tilde{\chi}_{st}$  and  $\tilde{\chi}$ , the former one used to parametrize the flamelet manifold, while the latter one is retrieved from the CFD calculation following Eq. (7)

$$\tilde{\chi} = C_\chi \frac{\epsilon}{k} \tilde{Z}^{\prime 2} \quad (7)$$

Turbulent-averaged values of any variable ( $\tilde{\psi}$ ) can be obtained according to Eq. (8).

$$\tilde{\psi}(\tilde{Z}, S, \tilde{\chi}_{st}, \tilde{t}) = \int_0^\infty \int_0^Z \psi(Z, \chi_{st}, \tilde{t}) P_Z(Z, \tilde{Z}, S) P_\chi(\chi_{st}, \tilde{\chi}_{st}, \sigma) dZ d\chi_{st} \quad (8)$$

In particular, the turbulent manifold stores turbulent-averaged values of relevant ‘k’ species in terms of average and variance of mixture fraction, average stoichiometric scalar dissipation rate and average normalized progress variable, i.e.  $\tilde{Y}_k = \tilde{Y}_k(\tilde{Z}, S, \tilde{\chi}_{st}, \tilde{c})$  using the formulation presented in Eq. (8). The lookup tables that compose the turbulent manifold are discretized with 51 points in  $\tilde{c}$ , 27 points in  $\tilde{\chi}_{st}$ , 41 points in  $\tilde{Z}$  and 17 points in  $S$ .

The coupling of UFPV and the CFD solver is performed by means of the chemical source term of the transport equation of any  $k$  species according to Eq. (9).

$$\tilde{\omega}_k = \frac{Y_k^{\text{tab}}(\tilde{Z}, S, \tilde{\chi}_{st}, \tilde{Y}_c(t + \Delta t)) - \tilde{Y}_k^{\text{cell}}(t)}{\Delta t} \quad (9)$$

where  $\Delta t$  is the CFD time-step, the species mass fraction at the cell is represented by  $\tilde{Y}_k^{\text{cell}}$  and is  $\tilde{Y}_k^{\text{tab}}$  is the species mass fraction tabulated in the next time step, for which  $\tilde{Y}_c(t + \Delta t)$  is calculated according to Eq. (10).

$$Y_c(t + \Delta t) = \tilde{Y}_c(t) + \tilde{\omega}_{Y_c}(\tilde{Z}, S, \tilde{\chi}_{st}, \tilde{Y}_c(t)) \Delta t \quad (10)$$

To reduce the computational cost, only a reduced number of the species in the chemical mechanism are transported by the CFD solver [24–26]. Some sink species are selected following the method presented in [27] to close the atomic mass balance, as well as to keep similar mixture thermophysical properties.

## 4. Results

This section is structured as follows: First, the results of closed homogeneous reactor and laminar flamelets are presented, focusing on the analysis of chemical kinetics and diffusion effects. Then, the mixing process at inert condition for OMEx-type fuels and n-dodecane is shown. After that, the analysis of the reactive spray for each fuel is presented. This analysis starts with global combustion parameters, followed by the autoignition sequence and eventually the flame structure at quasi-steady state. Although the main combustion analysis deals with  $OME_x$  and  $OME_1$ , some results for n-dodecane, standard fuel for ECN studies to highlight the differences between the oxygenated fuels and a more conventional hydrocarbon.

### 4.1. Closed homogeneous reactors

The first step in the analysis is the study of the chemical kinetics in closed homogeneous reactor conditions for all the fuels under investigation. This allows to compare the different chemical mechanism in terms of an ignition delay that is only influenced by chemical reactions. Ignition delay (ID) evolutions for three mechanism are shown in Fig. 2

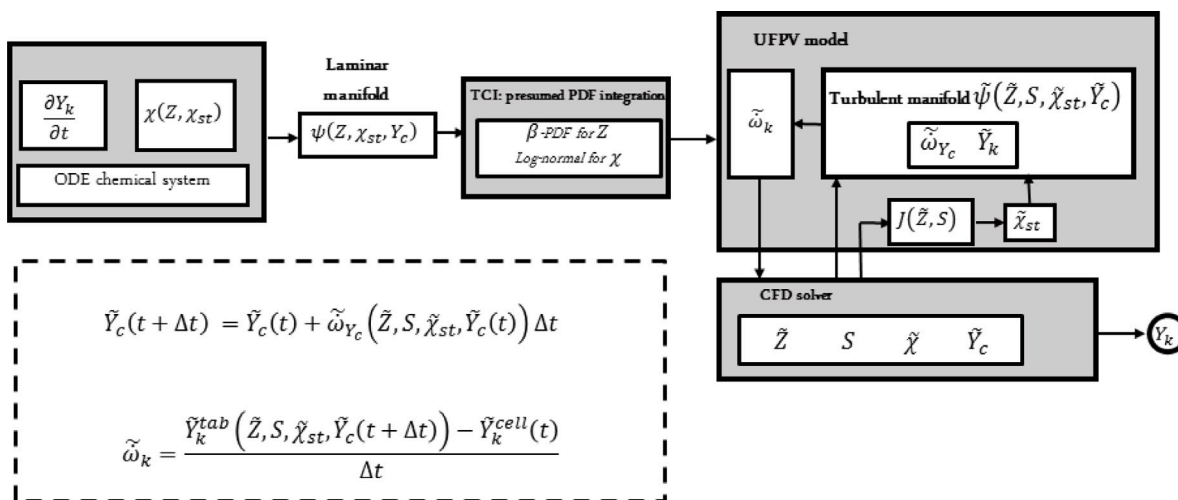


Fig. 1. UFPV model workflow [23].

as a function of mixture fraction ( $Z$ ) for baseline operating conditions (i.e. ambient temperature 900 K). Similarly to other hydrocarbon fuels, different zones can be identified along the ignition process depending on the reactivity state, namely those corresponding to the low and high temperature zones.

High-temperature ignition delay ( $ID_{HT}$ ) exhibits the typical v-shape for all three fuels as a function of mixture fraction, with a minimum value at the so-called ‘most reactive mixture fraction’ [28], which is relatively rich for all cases (0.059, 0.123 and 0.112 for *n*-dodecane,  $OME_x$  and  $OME_1$  respectively). As for the low-temperature ignition delay ( $ID_{LT}$ ), the v-shape is also visible spanning a wider mixture fraction range compared to the high-temperature one. However, differences among fuels are more evident, especially for *n*-dodecane and  $OME_x$ , where the minimum  $ID_{LT}$  is reached for very low mixture fractions, well in the lean region. The time elapsed between low and high temperature ignition delay ( $ID_{LT}$  and  $ID_{HT}$ ) is the cool flame period as defined e.g. Payri [29]. This is relatively long for the latter two fuels in the lean region. For  $OME_1$  this interval is overall short, hinting at a single-stage ignition process in most of ignition delay results shown which are in a relevant range in terms of spray ignition. Furthermore,  $OME_1$  presents longer ignition delay values than the other two fuels for both low and high temperature regimes. Finally, calculated ignition delays at the most reactive mixture fraction follow the trend presented by the cetane numbers in Table 1, with *n*-dodecane (0.23 ms) being the first one to ignite, closely followed by  $OME_x$  (0.32 ms), and finally  $OME_1$  shows the longest ignition delay (0.82 ms).

The chemical analysis of homogeneous reactors is complemented by the source term for the progress variable  $\dot{Y}_c$  over the mixture fraction–temperature map, Fig. 3. These maps show different reactivity islands depending on the mixture fraction and the distance to the equilibrium temperature, i.e. the progress variable. The same figures have been included in Appendix in terms of equivalence ratio (Fig. A.14), so that mixture composition compared to stoichiometry can be better compared. For all three fuels, a clear chemical activity region is found around stoichiometric locations and close to equilibrium temperatures (Region I). This island is narrower in terms of mixture fraction range for *n*-dodecane, compared to the oxygenated fuels. Just as an example, maximum  $\dot{Y}_c$  in this region is found at around 2000 K, ranging within  $0.045 < Z < 0.060$  for *n*-dodecane, while this range is  $0.085 < Z < 0.145$  for  $OME_x$  and  $0.085 < Z < 0.12$  for  $OME_1$ . A second intermediate island of reactivity (Region II) is found at around 1100 K for *n*-dodecane. While this happens at roughly below 1500 K for both  $OME_x$  and  $OME_1$ , it spans the mixture fraction range from almost zero to 0.3 for all three cases. This second reactivity island is very close to the initial adiabatic mixing curve for *n*-dodecane, so this will be the

trigger for initial reactions for the alkane fuel. For the two oxygenated fuels, the second island is further away from the initial inert state, but one can still find a third island (Region III) at or below 1000 K, with increasing  $\dot{Y}_c$  values as one moves towards rich regions.

Some of the differences from the ID plots can be explained based upon the  $\dot{Y}_c$  maps. As previously discussed, only two reactivity islands are observed for *n*-dodecane, which overlap for slightly lean to and rich mixtures ( $0.03 < Z < 0.1$ ), where  $ID_{HT}$  is shortest. Furthermore, the intermediate region between both islands, which would be representative of cool flame period, still exhibits a noticeable  $\dot{Y}_c$  value, and hence short differences between  $ID_{LT}$  and  $ID_{HT}$  (Fig. 2) are obtained within that range. Compared to the two other fuels, the intermediate reactivity island extends well into the lean region and very close to the adiabatic mixing, which results in a faster initiation of the low temperature chemistry reactions. However, no other reaction island is present in this range, which increases  $ID_{HT}$  (Fig. 2).

For  $OME_x$ , (Region III) is close to adiabatic mixing in the  $0.07 < Z < 0.15$  region, where low temperature ignition delay will be shortest (Fig. 2). Furthermore, for this mixture fraction range there is an overlap of three reactivity islands resulting in the lowest ignition delay, and a short duration of the cool flame period. In spite of the difference in reactivity distribution,  $ID$  values in this region are quite similar to those of *n*-dodecane, but the cool flame period is slightly longer due to the presence of a  $\dot{Y}_c$  valley at around 1000 K. Finally, in the  $Z < 0.07$  range (Region III) close to the adiabatic mixing line is similar to that of *n*-dodecane, but high temperature reactivity islands are weak or non-existent, and hence  $ID_{HT}$  is longer than for *n*-dodecane.

Finally,  $OME_1$  shows only the intermediate and high temperature reactivity islands (Region I and Region II).  $\dot{Y}_c$  values close to the adiabatic mixing line are lowest compared to the two other fuels, resulting in a very late initiation of reactions, and hence the longest  $ID$  values. Most of the ignition occurs in the  $0.05 < Z < 0.2$  range at relatively high temperature with an almost single step, as the short transition between  $ID_{LT}$  and  $ID_{HT}$  shows (Fig. 2).

#### 4.2. Laminar flamelets

The analysis of laminar igniting flamelets makes up the intermediate natural step to bridge the gap between the chemical analysis of homogeneous reactors and the spray problem. In fact, the initial evolution of a flamelet with the limit cases of a very low strain rate (SR) should be relatively close to a homogeneous reactor situation. As SR increases, the combustion process of the flamelet is increasingly affected by diffusion. Therefore, the relative roles of chemical reactivity and diffusion modify the ignition process.

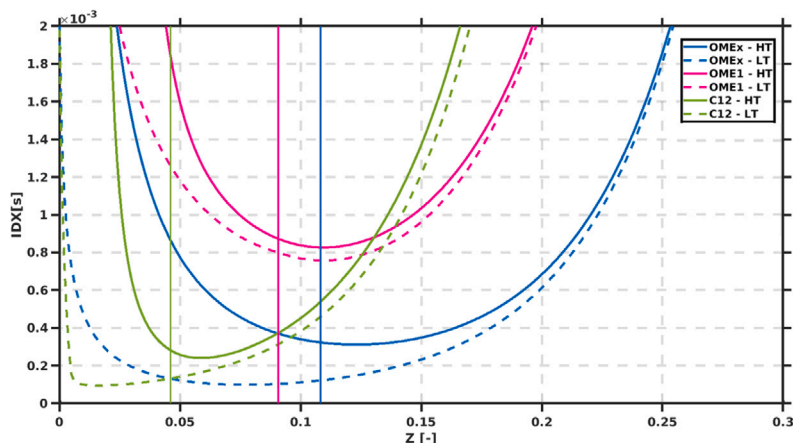


Fig. 2. Ignition delay for  $OME_x$ ,  $OME_1$  and n-dodecane (C12) for closed homogeneous reactors. Both low- (dashed line) and high-temperature stage (solid line) have been quantified. Starting conditions are obtained from an adiabatic mixing between fuel and air at nominal operating (ambient temperature 900 K). Vertical solid lines correspond to the stoichiometric mixture fraction  $Z_{st}$ .

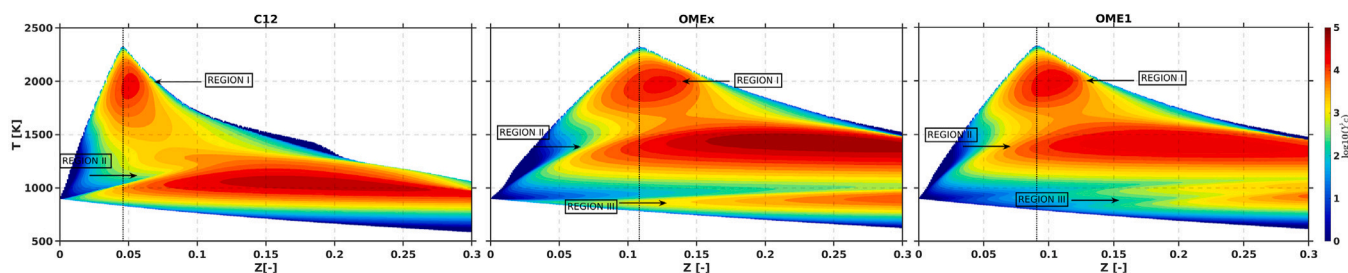


Fig. 3. Chemical source term  $\dot{Y}_c = dY_c/dt$  for homogeneous reactor calculations in terms of mixture fraction and temperature.

Fig. 4 shows the flamelet auto-ignition contour maps of  $\dot{Y}_c(T, Z)$  similarly to the homogeneous reactor (Fig. 3) for two different SR values, namely  $SR = 10$  and  $1000$  (1/s). A set of solid gray lines is superimposed on each case indicating instantaneous flamelet temperature with a constant  $10 \mu s$  time-step increase between lines. In that way, the density of lines is indicative of the progression rate of the autoignition sequence, e.g. temperature increases fast in the less dense region of the contour map. A dotted line is drawn to identify the maximum temperature at every time step, starting at the location where this maximum temperature is equal or higher than 905 K to identify the differences in the behavior of the first reactors. A solid black line identifies the steady solution.

In general terms, the most intense reactivity island at stoichiometric mixtures and high temperature is present for all cases, but clear differences can be observed in the intermediate and low temperature reactivity zones compared to Fig. 3. Starting with n-dodecane at the lowest strain rate value, one can find the reactivity zone associated to the low temperature, which ranges from very lean up to rich conditions  $0.025 < Z < 0.1$ . Moving towards high temperature, a drop in reactivity is observed at around 1000 K, similarly to the homogeneous reactors, followed by the final high reactivity around stoichiometric conditions. The high reactivity island observed at rich mixtures ( $Z > 0.1$ ) in homogeneous reactors (Region II) is not present here. This could be due to the effect of diffusion at richer mixtures in mixture fraction space, as the imposed profile of scalar dissipation rate increases with mixture fraction in the plotted range. Note that this diffusion effect is the result of both convection and diffusion in physical space.

For the  $OME_x$  case, a low intensity zone is observed close to the initial adiabatic mixing line, especially around the stoichiometric-rich zones, which was already present in homogeneous reactors. Moving to higher temperature, the drop in chemical activity is seen up to 1000–1100 K, followed by a reactivity pattern similar to that of homogeneous

reactors at high temperature, with two zones separated by a small valley at around 1500 K leading up to the steady solution. The peak reactivity zone observed for homogeneous reactors at rich conditions ( $0.15 < Z < 0.3$ ) and below 1500 K (Region II) vanishes at low SR, although it can again be observed at the high one.

When moving to  $OME_1$  the reactivity zone close to the adiabatic mixing line disappears, consistently with the long  $ID_{LT}$ , and the middle zone island is narrower in terms of mixture fraction range compared to homogeneous reactors in Fig. 3. Similarly to  $OME_x$ , no presence of the rich reactive zone is seen for low SR, while it appears again at high SR.

In general terms, a higher strain tends to shift reactivity towards richer mixtures. This is specially evident for both oxygenated fuels and for the intermediate-high temperature reactivity islands, which tend to expand within the mixture fraction space.

The overlap of instantaneous and maximum temperature lines superimposed upon reactivity contours helps explain the temporal evolution of flamelet ignition. For all three fuels, ignition is seen to start at lean conditions, shifting towards rich mixtures along the low reactivity zone at around 1000 K with a very small temperature increase. For low SR the flame reaches the intermediate reactivity island, after which a very steep temperature increase is observed towards the steady state, which is evidenced by the apparent decrease in the density of instantaneous temperature lines around the maximum temperature line. As SR increases, diffusion effects tend to propagate ignition from the most reactive mixture fraction to other mixtures, both on the rich and lean sides. This is evidenced by the wider profiles of the instantaneous temperatures in mixture fraction space.

Fig. 5 compares the evolution of  $T_{max}$  against mixture fraction (left) and time (right). The left plot is also included in Appendix in terms of equivalence ratio, Fig. A.15. For n-dodecane, one can observe the typical time evolution of a two-stage ignition process. The initial cool flame can be identified independently of SR by a clear drop in the

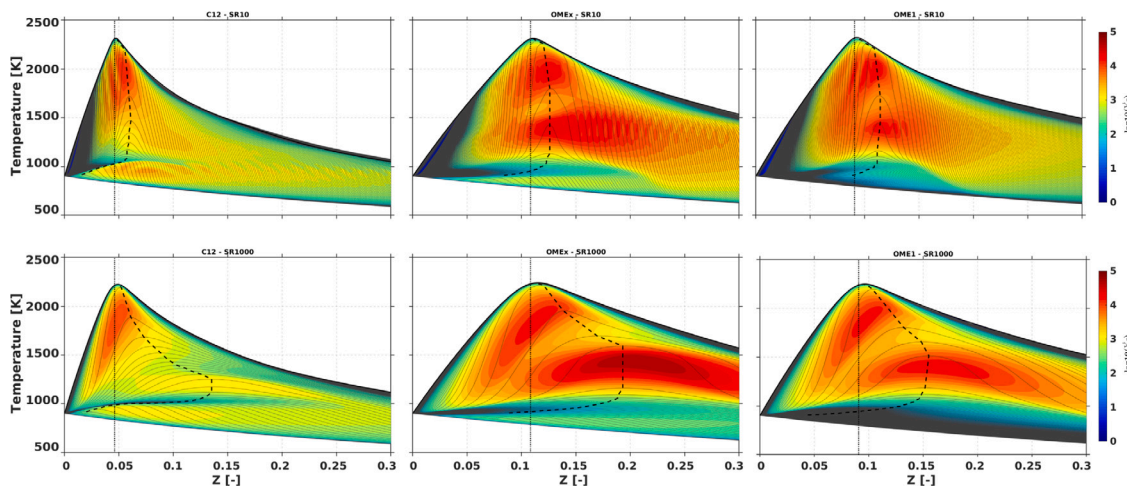


Fig. 4. Contours of  $\dot{Y}_c = \partial Y_c / \partial t$  from laminar flamelet solver in terms of mixture fraction and temperature. Superimposed on the contours, instantaneous flamelet temperature distributions (solid lines) with  $10 \mu s$  timestep have been plotted, together with the evolution of maximum temperature at every timestep (dashed lines). Top row corresponds to  $SR = 10(1/s)$ , bottom row to  $SR = 1000(1/s)$ . Left column corresponds to n-dodecane, middle  $OME_x$  and right  $OME_1$ .

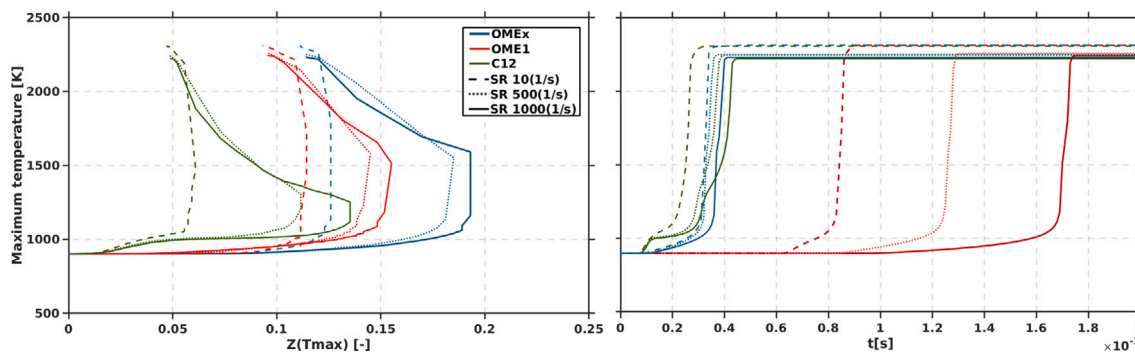


Fig. 5. Evolution of maximum temperature in the flamelet during autoignition against time (right) and against the mixture fraction value at which it occurs for dodecane,  $OME_x$  and  $OME_1$  at three strain rate values, namely 10, 500 and 1000 (1/s).

slope of the maximum temperature for some period until the final jump at high temperature ignition timing occurs. This is not quite the case for  $OME_1$ , which aside from showing a later increase in temperature also features a more progressive initial temperature increase without an explicit drop in slope. After reaching around 1100 K, the second-high temperature increase is observed.  $OME_x$  shows an intermediate behavior with a timing similar to that of n-dodecane, and at the same time a more steady initial temperature increase. This evidences that such oxygenated fuels are closer to a single-stage ignition process.

For n-dodecane, increasing SR does not have any effect on the initial low temperature rise, while it tends to delay high temperature ignition. Another clear effect of increasing SR is the shift of the subsequent temperature rise towards rich mixtures. The steep temperature increase at constant mixture fraction only proceeds until reaching a point from which maximum temperature shifts back towards lower mixture fraction values. This turning point coincides with the high temperature limit of the reactivity island at rich location ( $0.1 < Z < 0.2$ ) (Fig. 4). After that, maximum temperature eventually reaches the stoichiometric high reactivity region, where evolution becomes steady. For medium and high strain rate, this results in an apparent 3-stage ignition of maximum temperature versus time, namely the initial low temperature increase, the steep increase at constant mixture fraction in the rich region and the final temperature increase when reactivity shifts back towards stoichiometry. This behavior is not observed for low strain rates, where high temperature ignition occurs almost at stoichiometric conditions. Some of the previous effects can be discussed for the oxygenated fuels:

- Little effect of SR is observed on the timing of the low temperature ignition phase for  $OME_x$ , while it tends to delay the high temperature phase. In the early ignition stages, gradients of species are small and hence SR does not have a strong effect. It must be highlighted that a lower sensitivity of  $OME_x$  to strain is observed compared to n-dodecane, which results in a faster high temperature ignition of the latter fuel versus n-dodecane at the highest SR, compared to the slower ignition at low SR. As for  $OME_1$ , the much lower reactivity results in a high sensitivity to strain for both the low and high temperature ignition stages.
- For both oxygenated fuels maximum temperature evolution in the mixture fraction space also shows that ignition occurs at richer mixtures as SR increases. A similar behavior to that of n-dodecane is also observed, with also a steep increase to a constant mixture fraction followed by a shift of maximum temperature back to stoichiometric mixtures. However, for oxygenated fuels the latter phase starts at a higher temperature and closer to stoichiometric conditions, in agreement with the important reactivity island at rich locations (Fig. 4).

In this section the auto-ignition process of the flamelets of the three fuels has been described. Important differences among them have been found, namely the absence of the zone of reactivity associated with low temperature in oxygenated fuels, as well as the presence of an important reactivity zone at intermediate temperature, not present in n-dodecane. Ignition characteristics of  $OME_x$  are at an intermediate situation between n-dodecane and  $OME_1$ .

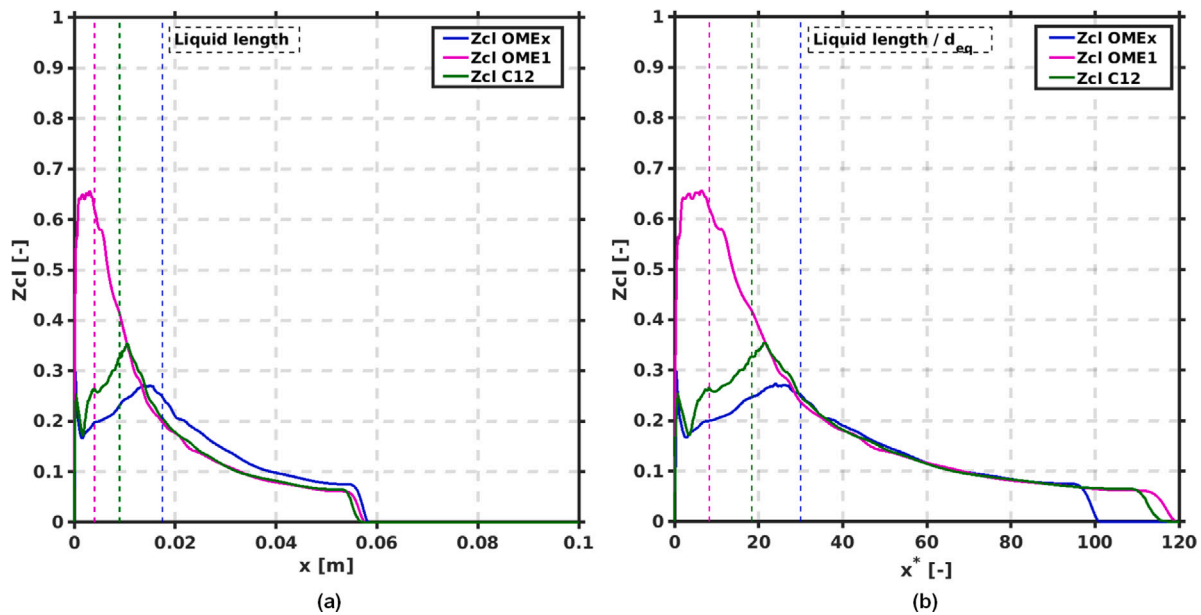


Fig. 6. Mixture fraction profiles on the spray axis at 1.5 ms vs. axial distance (a) and vs normalized axial distance (b) for the nominal inert condition. Vertical dashed lines show the location where maximum liquid length is found.

### 4.3. Inert spray mixing characteristics

In order to isolate the mixing process of the combustion effects, inert cases have been calculated. Previous work developed for the group showed the validation of the model setup for n-dodecane [16]. Fig. 6a shows the evolution of the mixture fraction on the spray centerline for n-dodecane [16],  $OME_x$  and  $OME_1$  for nominal Spray A conditions. Results show that the evolution is quite similar for all three fuels, with different plots peaking close to the location where the maximum liquid length is found, an drooping downstream with the typical  $x^{-1}$  law. Mixture fraction is very similar between n-dodecane and  $OME_1$  from 10 mm up to the tip of the jet, while  $OME_x$  shows slightly higher mixture fraction values. Fig. 6b shows the mixture fraction evolution on the centerline versus the axial coordinate normalized by the equivalent diameter of each fuel,  $x^* = x/d_{eq}$ . The equivalent diameter is defined according to Eq. (11).

$$d_{eq} = d_o \sqrt{\frac{\rho_f}{\rho_a}} \quad (11)$$

where  $d_o$  stands for the nozzle effective diameter, and  $\rho_f$  and  $\rho_a$  correspond to fuel and air density. Starting from n-dodecane, fuel density increases 15% and 40% when moving to  $OME_1$  and  $OME_x$ , respectively (Table 1), while all other parameters are constant. The normalized plot evidences that the scaling law is adequate, and that the only differences among mixture fraction distribution downstream of the liquid length are due to the effect of fuel density, in agreement with previous knowledge from mixing-controlled turbulent sprays. Therefore, mixture fraction distribution for  $OME_1$  is essentially coincident with that of n-dodecane [16], and  $OME_x$  will have a slightly higher mixture fraction values due to the higher density. Inert calculations were not extended to other ambient temperature cases, but if one accounts for the scaling parameter, mixing distribution should be the same, as the temperature sweep has been carried out at constant ambient density. The only expected difference will be related to maximum liquid length, but due to the relatively high volatility of these fuels, no other major differences are expected.

### 4.4. Global combustion parameters

In the present section, predicted combustion global parameters for  $OME_x$  and  $OME_1$ , namely tip penetration and lift-off length results

are presented to give an overview of the prediction capabilities of the modeling approach. Numerical results are compared to those obtained from experiments for validation purposes. Tip penetration and ignition delay (ID) are determined from schlieren, and lift-off length (LOL) is obtained from  $OH^*$  chemiluminescence [8]. On the CFD side, ECN recommendations are followed. Tip penetration is define as the axial distance from the nozzle to the maximum location where mixture fraction reaches a value of 0.001, ID is defined as the time elapsed from the start of injection to the point where the maximum derivative of the maximum of temperature in the domain is achieved, and LOL is defined as the minimum axial distance from the nozzle to the closest location where 14% of the maximum value of the mass fraction of OH in the domain is reached.

The time evolution of tip penetration and lift-off length for both fuels and the different temperature values is shown in Fig. 7. Results show the steadily increasing tip penetration with time, while lift-off length is observed starting from ignition delay, with an initially decreasing evolution until a quasi-steady value is reached. Tip penetration evolution coincides with previous experimental and numerical results in the literature [30–33] progressing with the well-known inert evolution from the start of injection until some time after ID. At ignition timing, the jet expands radially, and there is a reorganization of the flow during which tip penetration does not depart from the inert one. Once this flow reorganization occurs, tip penetration accelerates and proceeds faster than the inert case.

For the investigated temperature sweep, tip penetration of all three temperature cases overlap for timings before ID. This parameter is governed by nozzle momentum flux and ambient density, which are all constant. The overlap continues until some period after ignition, from which tip penetration acceleration eventually occurs. Acceleration occurs later with lower ambient temperature, concurrently with the stabilization of LOL further away from the nozzle [34]. For the  $OME_x$  800 K case, ID is around 4 times longer than for 900 K and 6 times longer than for 1000 K. This results in an almost inert tip penetration until 1.2 ms for the 800 K case, at a much lower rate compared to the two other cases. A similar conclusion can be derived for  $OME_1$  cases.

Predicted tip penetration for  $OME_x$  (Fig. 7, left) agrees with experiments until ignition timing, after which a slight overprediction is obtained for 900 and 1000 K, and satisfactory agreement is observed for the 800 K case. Lift-off length predictions for  $OME_x$  also match

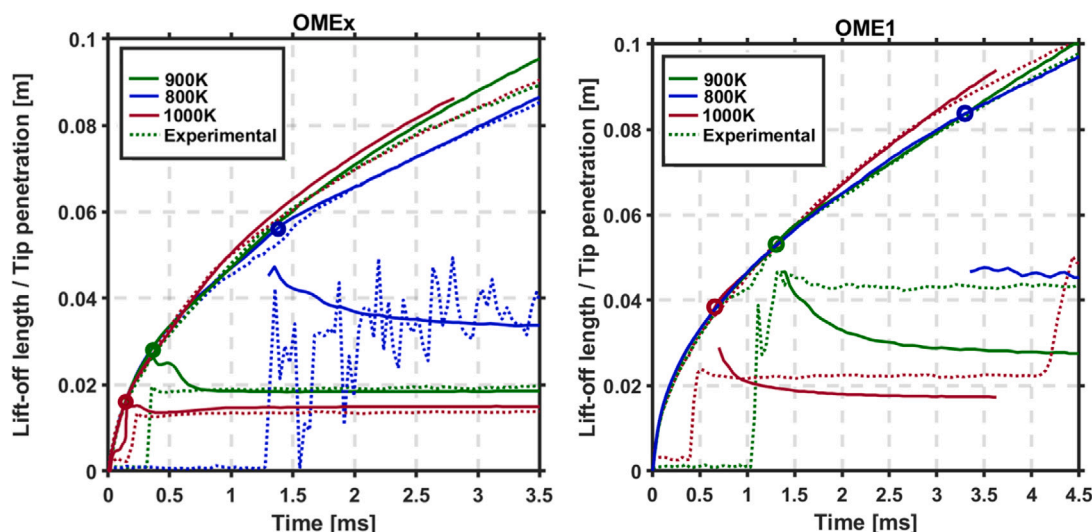


Fig. 7. Time evolution of tip penetration and lift-off length for  $OME_x$  (left) and  $OME_1$  (right). Marker shows the ID timing as derived from CFD calculations.

Table 3

Ignition delay and stabilized lift-off length for both experimental results and CFD calculations. Experimental data include both average and standard deviation.

	800 K		900 K		1000 K	
	Experiments	CFD	Experiments	CFD	Experiments	CFD
$ID_{OME_x}$ [ms]	$1.21 \pm 0.08$	1.26	$0.33 \pm 0.02$	0.34	$0.19 \pm 0.01$	0.18
$ID_{OME_1}$ [ms]	–	3.30	$1.20 \pm 0.08$	1.31	$0.45 \pm 0.03$	0.66
$LOL_{OME_x}$ [m]	$0.037 \pm 0.022$	0.034	$0.019 \pm 0.0008$	0.020	$0.0140 \pm 0.0005$	0.015
$LOL_{OME_1}$ [m]	–	0.050	$0.040 \pm 0.002$	0.030	$0.020 \pm 0.001$	0.020

experimental values, especially in the quasi-steady state. ID and quasi-steady LOL values are presented in Table 3, confirming the good agreement between experiments and simulations for all temperatures values.

Fig. 7 (right) also shows spray tip penetration and lift-off length for  $OME_1$  at the three ambient temperature conditions. The overall evolution is essentially the same until ID, but this characteristic timing is reached later due to the lower reactivity of  $OME_1$ . After ID, spray tip acceleration is also observed, with differences among conditions depending on the ignition timing. Lift-off length is also observed to stabilize further away from the nozzle compared to  $OME_x$ . Comparison between simulation and experimental results show excellent agreement for tip penetration, while predicted lift-off length presents a strong flame recession at 900 and 1000 K, which is not observed in experimental results. This results in an under-predicted stabilized value of the lift-off length, which is noticeable at the highest temperature and becomes much more evident at the nominal one. It must be noted that no ignition was obtained in the experiments for 800 K. This behavior was not reproduced by the numerical results, where a very late ignition was obtained at 3.3 ms. However, numerical results for 800 K are presented for substantiation of the obtained flame topology in later sections. Additionally, ignition delay and stabilized lift-off length value are presented in Table 3. Ignition timing is also properly captured by CFD, while quasi-steady lift-off is underpredicted, as previously discussed.

Differences between both fuels are obviously linked to the fuel reactivity characteristics, which have been discussed in previous sections at flamelet level. Subsequent section will discuss the spray ignition sequence to help draw an overall picture of the combustion characteristics of both fuels.

#### 4.5. Autoignition sequence

This section describes the analysis of autoignition in terms of rate of heat release and mass species, both in terms of the spatial and temporal

evolution. Previous results have shown that 1000 and 900 K exhibit a very similar tip evolution, ignition timing and LOL stabilization. Therefore, only the sequence corresponding to 900 and 800 K is presented for both  $OME_x$  and  $OME_1$ . Starting for the nominal condition (900 K) for  $OME_x$ , Fig. 8 shows the fields of local heat release rate (right panel) and mass fraction of  $CH_2O$  and OH (left panel). These two species are used as tracers for low and high temperature ignition, respectively. Keeping in mind that modeled ID for this case is 0.344 ms, several time instants have been selected around this timing to describe the auto-ignition sequence. Contours show the appearance of  $CH_2O$  at the same time (0.22 ms) as the low temperature heat release rate begins to rise mildly. This is consistent with the concept of using  $CH_2O$  as a tracer of the low temperature ignition. As time advances, the spray is seen to grow both in axial and radial directions. Starting at 0.38 ms, which is the first frame after ID (0.344 ms), a noticeable increase in OH mass fraction can be observed, concurrent with a drop in total  $CH_2O$  as well as a sharp increase in heat release rate. Both OH and the most intense heat release are located at the tip of the spray.

Once ID timing is elapsed, the flame progress and develops into a typical diffusion structure, with  $CH_2O$  distributed around the center of the spray and OH mainly on the stoichiometric reacting surface. Both the total mass of  $CH_2O$  and the heat release rate stabilize, while OH mass increases due to the elongation of the diffusion flame front. The overall species distribution is similar to that presented in [16] for n-dodecane at the same operating conditions, hinting at a very similar flame topology for  $OME_x$  and regular hydrocarbons.

Fig. 9 shows the ignition sequence for the lower temperature case (800 K). Spray tip is observed to be longer than for the nominal case due to the later ignition timing. However, the stoichiometric surface does not increase with the spray tip, but becomes stabilized with a maximum length of 40 mm after 0.86 ms. This behavior creates a lean region between the stoichiometric surface and the tip of the spray where ignition is seen to occur.

A very different distribution of species and heat release is found during ignition.  $CH_2O$  is seen to be relatively uniformly distributed



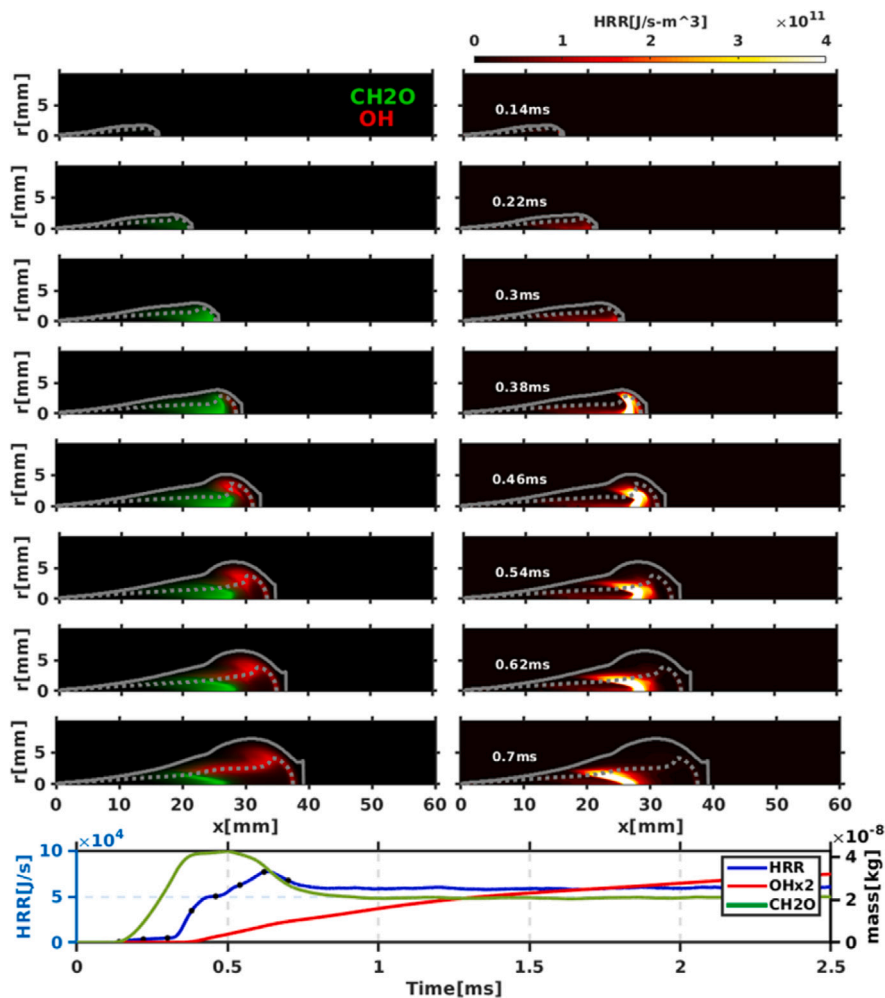


Fig. 8. Time sequence of CH<sub>2</sub>O and OH mass fraction (left panel) and local heat release rate (right panel) around ignition timing for *OME<sub>x</sub>* at 900 K. Colorscales are normalized to the instantaneous maximum. Spray radius and stoichiometric mixture fraction isocontour are marked with solid and dotted lines, respectively. Bottom plot shows the time-resolved maximum values of mass fraction and heat release rate. (For interpretation of the references to color in this figure legend, the reader is referred to the web version of this article.)

throughout the whole spray width until 1.22 ms, after which both heat release and OH appear at the very tip of the jet. This ignition site later recedes towards the orifice, as seen both in heat release and OH along the different timings until 1.7 ms. At that timing, heat release rate is seen to start from a region at around  $x = 35$  mm close to the spray radius and extends almost linearly towards the spray center, which is reached at around  $x = 47$  mm, where the maximum OH values are found. Note that a detailed inspection shows that maximum OH is not always coincident with maximum heat release locations. Heat release rate layer is close to the stoichiometric surface but clearly on the lean side. Compared to the nominal temperature, flame ignition occurs under lean conditions, which is rarely found in Diesel-like sprays.

Fig. 10 shows the autoignition sequence for *OME<sub>1</sub>* at 900 K, which is quite different to the corresponding *OME<sub>x</sub>* condition. Contours show actually more similar features to those of the low temperature 800 K *OME<sub>x</sub>* case. CH<sub>2</sub>O is uniformly distributed before 1.28 ms, with absence of low-temperature heat release. OH is first observed between 1.28 and 1.4 ms at the tip of the jet, concurrently with a sharp increase in both local and global heat release rate, from which it later recedes towards the nozzle. Similarly to the 800 K *OME<sub>x</sub>* case, high temperature ignition is seen to occur in a lean region outside of the stoichiometric surface, which remains steady from the first instant until being reached by the later heat release recession at 1.52 ms. After that, stoichiometric surface increases in length due to the lower entrainment linked to the drop in local density, and it ends up interacting with the heat release front. The last frame shows a heat release rate front anchored at the

tip of the stoichiometric surface, with OH located further downstream under lean conditions.

Due to the particular flame structure developed by *OME<sub>1</sub>*, it is also interesting to show the auto-ignition sequence of the case with the lowest ambient temperature, Fig. 11. It is worth reminding the fact that, based on experimental results [8], *OME<sub>1</sub>* did not ignite at this operating condition, but CFD calculations predicted reaction onset. In this case, the analysis of species and local heat release shows a similar sequence to that at 900 K (CH<sub>2</sub>O uniformly distributed, high temperature ignition occurring at the jet tip and the reaction zone receding towards the orifice until stabilization). However, both ignition and flame stabilization occur later in time and further away from the orifice. Furthermore, the observed recession of the reaction zone after ignition does not reach the stoichiometric surface, and hence the reaction zone always occurs under lean conditions.

Finally, Fig. 12 shows the evolution of the maximum temperature in the CFD domain at each time step against the mixture fraction value at which this occurs. The layout is then very similar to the one used for the laminar flamelets (Fig. 5). *OME<sub>x</sub>* at 900 K presents a similar autoignition sequence as in flamelets, with an initially lean low temperature ignition that propagates to rich mixtures, where it eventually runs into the high temperature phase. This is also similar to the typical ignition sequence for n-dodecane. For all other three cases, namely *OME<sub>x</sub>* at 800 K, and *OME<sub>1</sub>* at 800, 900 K, the evolution is quite different, with chemical activity always proceeding at lean conditions.

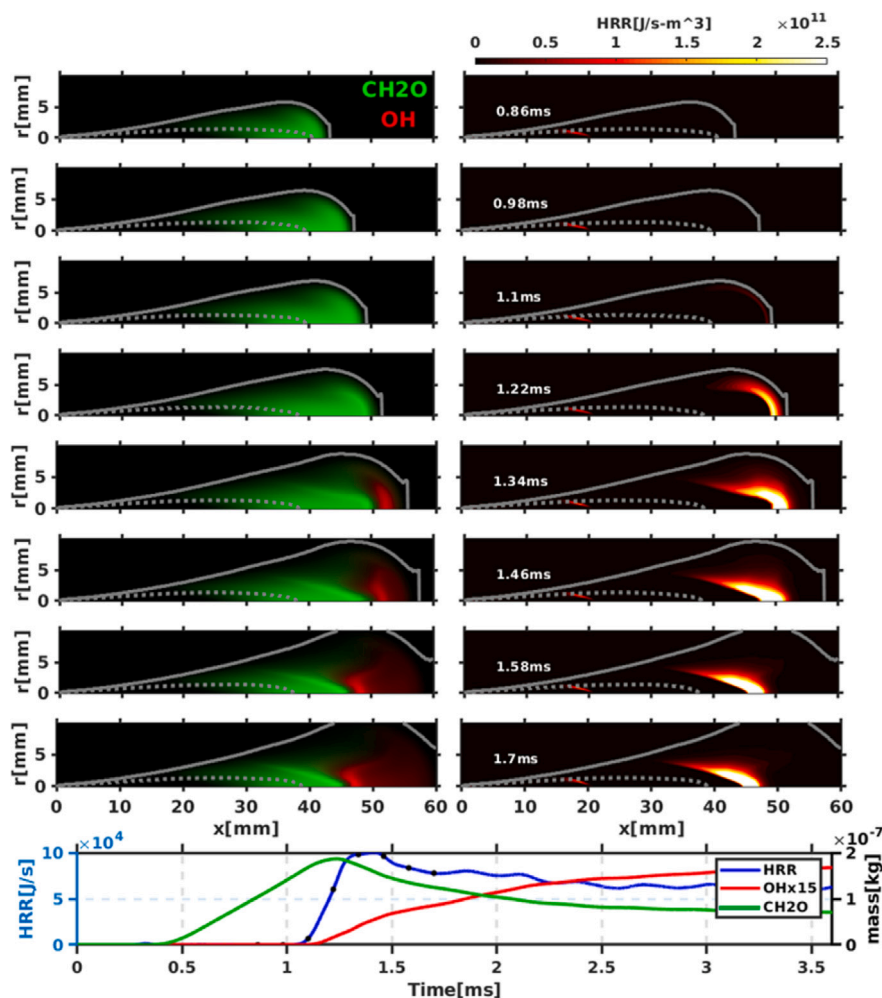


Fig. 9. Time sequence of CH<sub>2</sub>O and OH mass fraction (left panel) and local heat release rate (right panel) around ignition timing for OME<sub>x</sub> at 800 K. Colorscales are normalized to the instantaneous maximum. Spray radius and stoichiometric mixture fraction isocontour are marked with solid and dotted lines, respectively. Bottom plot shows the time-resolved maximum values of mass fraction and heat release rate. (For interpretation of the references to color in this figure legend, the reader is referred to the web version of this article.)

They are examples where laminar flamelet ignition sequence is not quite the same as that of spray.

To give a first explanation of the difference in the ignition sequence between flamelets and sprays, one can resort to the residence time, which can be defined as the amount of time spent by the fuel at a given mixture fraction/equivalence ratio value. The mixing field in flamelet space can be considered as having an infinite residence time, in the sense that all mixture fraction values are present from the initial time, while in the spray cases the mixing field develops with time. As shown in [16], residence time changes along iso-lines of mixture fraction, and it increases when moving downstream and further way from the axis. This finite residence time has strong implications on how reaction develops in mixture fraction space versus spray calculations, and can be considered as a first factor explaining differences between Figs. 12 and 5.

#### 4.6. Quasi-steady flame structure

In this section, the effect of ambient temperature on the flame structure is analyzed at quasi-steady state for both fuels and all temperature conditions. Fig. 13 shows spatial distribution of heat release rate (left), scaled mass fractions of CH<sub>2</sub>O and OH (middle) as well as normalized progress variable (right). The spray radius is plotted with gray solid line, the blue vertical line indicates the LOL position and

the stoichiometric mixture fraction is plotted with a dashed gray line as in Fig. 8.

Starting with OME<sub>x</sub> at 900 K, a heat release rate zone is observed at the flame base upstream of the LOL region, which can be associated to the low temperature ignition stages. Then, an intense heat release zone is found at the lift-off location, and further downstream heat release is found on the stoichiometric surface. This structure is very similar to n-dodecane cases shown in [16]. As for species, CH<sub>2</sub>O is first found slightly upstream of the lift-off length location and extending towards the spray centerline, always within rich mixtures, while OH is found on top of the stoichiometric surface, where the diffusion flame high temperature reaction occurs. The spatial distribution of species has good correlation with recent experimental results [10] obtained by measuring CH<sub>2</sub>O and OH radical distributions using planar Laser-Induced Fluorescence techniques. Moving to 1000 K, the quasi-steady flame topology remains very similar to that of the nominal temperature, except for the reduction in LOL. A typical diffusion flame is still observed, very similar to n-dodecane case in [16].

On the other hand, the bottom panel shows local heat release rate for the 800 K case. The long LOL and concurrently short stoichiometric surface implies that local heat release is only present at around the lift-off location, with no further reaction on the downstream part of the stoichiometric surface. This heat release structure can be seen to modify the spatial distribution of the relevant species. CH<sub>2</sub>O is seen to be present much extensively upstream of the lift-off location, while

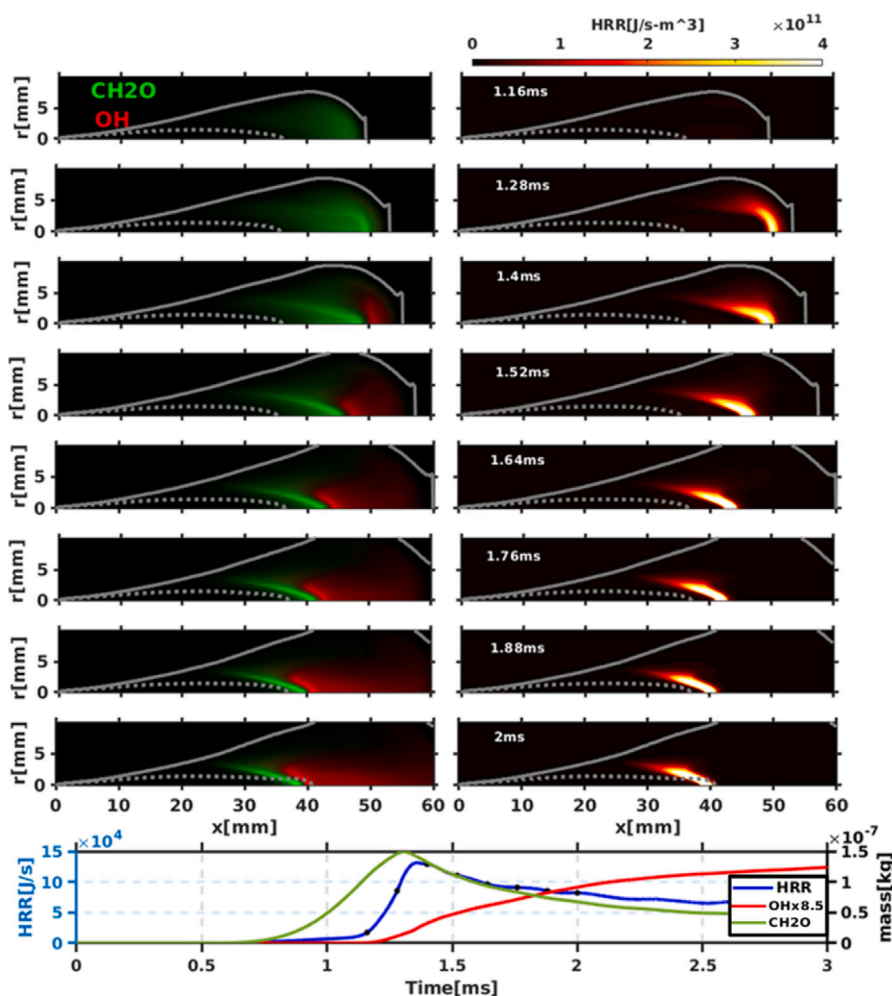


Fig. 10. Time sequence of  $\text{CH}_2\text{O}$  and  $\text{OH}$  mass fraction (left panel) and local heat release rate (right panel) around ignition timing for  $\text{OME}_1$  at 900 K. Colorscales are normalized to the instantaneous maximum. Spray radius and stoichiometric mixture fraction isocontour are marked with solid and dotted lines, respectively. Bottom plot shows the time-resolved maximum values of mass fraction and heat release rate. (For interpretation of the references to color in this figure legend, the reader is referred to the web version of this article.)

$\text{OH}$  is essentially located downstream of the  $\text{CH}_2\text{O}$  surface, instead of extending on the stoichiometric surface. The flame topology under quasi-steady conditions, hence, is governed by the presence of a highly premixed reaction front at the very tip of the stoichiometric surface.

Finally in the right panel, the normalized progress variable  $C$  field is shown. This variable indicates when the reaction state reaches steady conditions. Similarly to both heat release and relevant species, no big differences are found between 900 K and 1000 K, where the transition towards equilibrium values occurs at the lift-off length throughout the whole radial cross-section. At 800 K, however, a fast transition is seen at the tip of the stoichiometric surface, but this transition is more gradual at radial locations higher than the stoichiometric ones, hinting at a lower reactivity within such lean locations.

Fig. 13 also shows results at quasi-steady state for  $\text{OME}_1$ . Overall, the case at 1000 K is quite similar to those for  $\text{OME}_x$  at 900 and 1000 K, i.e. a typical lifted diffusion flame with the intense heat release rate starting at the lift-off and extending along the stoichiometric surface. For  $\text{OME}_1$  the stoichiometric surface stabilizes closer to the nozzle compared to  $\text{OME}_x$ . This is mainly due to the lower fuel density, as the analysis of the inert spray distribution in Section 4.3 has shown. The distribution of both relevant species and progress variable is also overall similar to the corresponding  $\text{OME}_x$  cases.

On the other hand, results at 900 and 800 K are more similar to the 800 K  $\text{OME}_x$  case, showing a lift-off length stabilizing close to (900 K) or downstream (800 K) the tip of the stoichiometric surface. In fact, the  $\text{OME}_x$  case at 900 K seems to be an intermediate situation

between the  $\text{OME}_1$  cases at 900 K and 800 K. The reduction in reactivity due to a low ambient temperature or a low reactive fuel evidence similar effects, i.e. it shifts the lift-off length downstream, which for these oxygenated fuels strongly interacts with an intrinsically short stoichiometric surface. This displaces the main reaction zone further downstream and eventually, a lean mixing-controlled flame is obtained, with the reaction zone happening at equivalence ratio below 0.72. This behavior is also reflected in the spatial distribution of relevant species and progress variable. In the latter case, the normalized progress has a more gradual transition towards steady conditions, quite different from the typical diffusion flame. Although not shown here, the maximum temperature of the 800 K case will be dictated by that of the lean premixed front, which could have advantages in terms of  $\text{NO}_x$  formation.

For both fuels and all temperature cases, the evolution of the normalized progress variable around the lift-off location shows that  $\text{CH}_2\text{O}$  peak values are found at locations where progress variable starts to rise, while  $\text{OH}$  tends to occur in locations where progress variable is close to the steady value. Further detailed analysis (plot are omitted here for brevity reasons) indicates that for the low temperature cases, where the flame front is in fully lean regions, peak heat release rate occurs in locations concurrent with high  $\text{CH}_2\text{O}$  concentrations, and not with high  $\text{OH}$ , which is usually the case when a diffusion flame front exists.

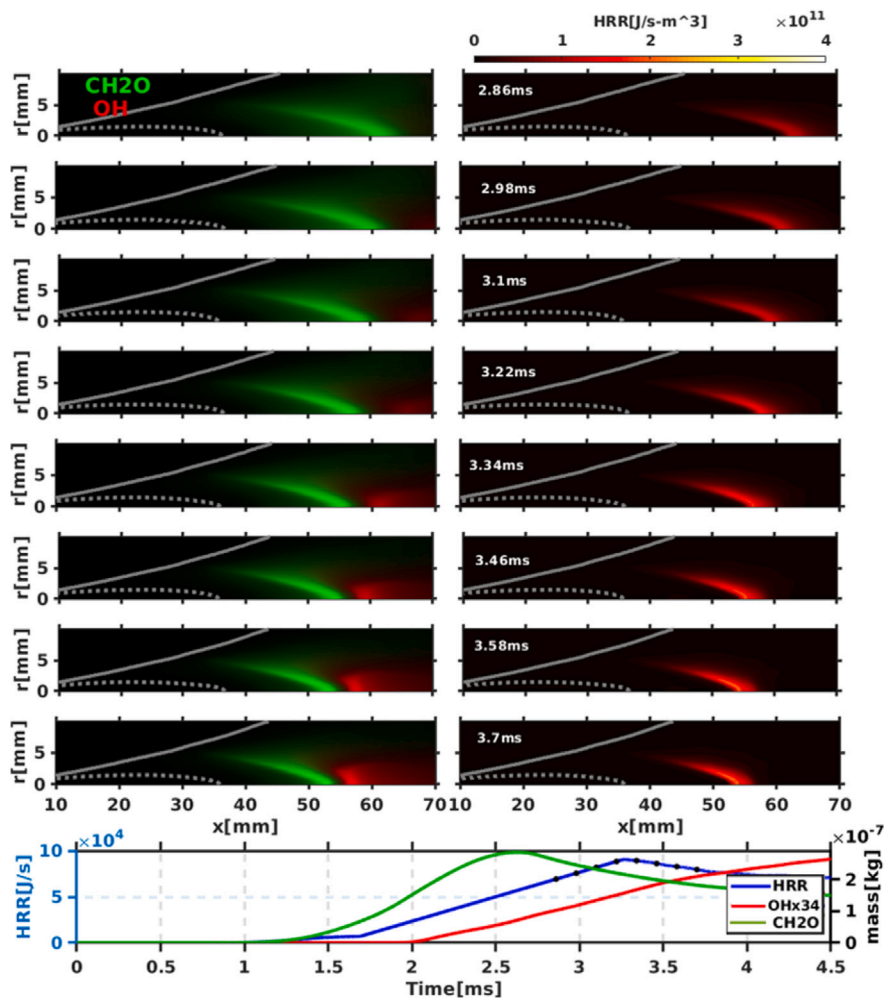


Fig. 11. Time sequence of CH<sub>2</sub>O and OH mass fraction (left panel) and local heat release rate (right panel) around ignition timing for *OME*<sub>1</sub> at 800 K. Colorscales are normalized to the instantaneous maximum. Spray radius and stoichiometric mixture fraction isocontour are marked with solid and dotted lines, respectively. Bottom plot shows the time-resolved maximum values of mass fraction and heat release rate. (For interpretation of the references to color in this figure legend, the reader is referred to the web version of this article.)

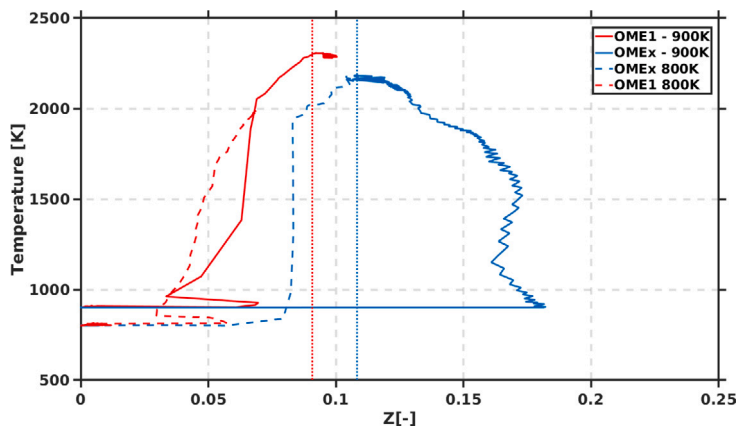


Fig. 12. Evolution of instantaneous maximum temperature along ignition as a function of mixture fraction as derived from CFD results for both oxygenated fuels at 800 and 900 K.

5. Conclusions

The combustion process and flame topology for isolated liquid sprays have been computationally studied for two oxygenated and renewable fuels, namely *OME*<sub>x</sub> and *OME*<sub>1</sub>, under ECN Spray A conditions. Three ambient temperature levels have been evaluated, and results have been compared to those available in experiments. Through

the analysis of homogeneous reactor, flamelets and spray calculations, the following conclusions have been derived:

- Homogeneous reactors evidence differences in reactivity in terms of ignition delay and mixture fraction. Ignition delay for *OME*<sub>x</sub> shows a similar behavior to that of n-dodecane, for both low and high temperature paths. *OME*<sub>1</sub> ignition, however, is slower

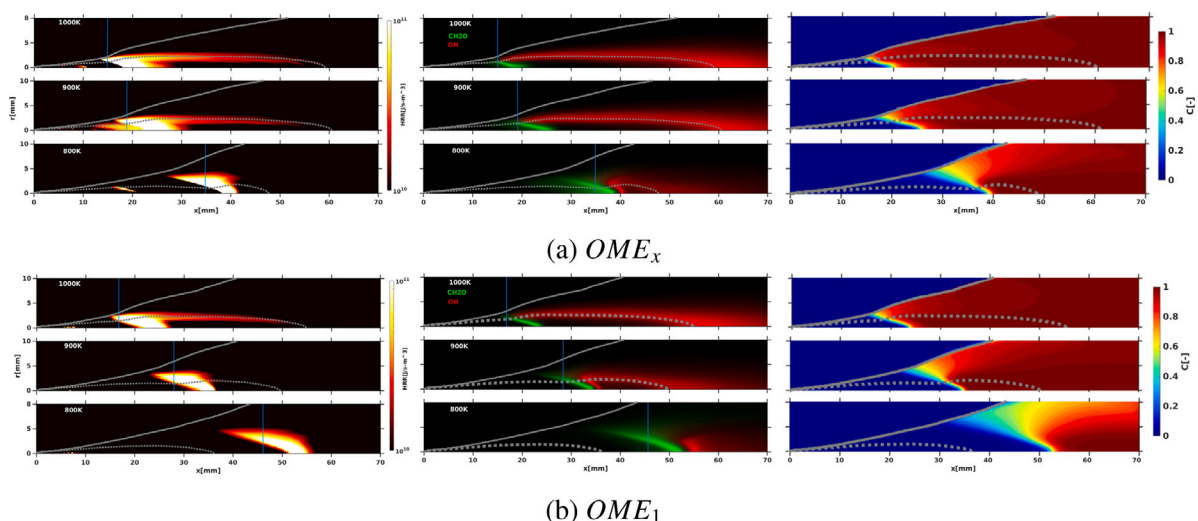


**Fig. 13.** Quasi-steady local HRR contour (left), normalized  $CH_2O$  and  $OH$  mass fractions (middle) and normalized progress variable (right) at ambient temperature of 800 K (bottom), 900 K (middle) and 1000 K (top) for (a)  $OME_x$  and (b)  $OME_1$ . Solid gray line represent the spray radius, dashed green line drawn at  $\phi = 1$  and the corresponding lift-off length of each case is showed with the blue vertical line. (For interpretation of the references to color in this figure legend, the reader is referred to the web version of this article.)

than the other two, consistently with the lower cetane numbers. For both fuels, the most reactive mixture fraction is slightly rich, similarly to n-dodecane.

- Laminar flamelets have shown the effect of diffusion on reactivity, which is later translated to the spray calculations. Compared to n-dodecane, oxygenated fuels tend to show lower reaction rate close to the initial adiabatic mixing conditions. The ignition sequence, described in terms of maximum temperature, shows a similar path to n-dodecane, with an initially lean low temperature ignition followed by the transition to high temperature ignition for rich conditions. Two important differences are to be noted. The first one is the absence of strong low temperature ignition for the oxygenated fuels, especially when compared to n-dodecane. The second one is the effect of diffusion, which scales with strain rate and may eventually result in faster ignition for  $OME_x$  compared to n-dodecane, although in the homogeneous reactor calculations the results were opposite. This highlights the effect of diffusion on ignition.
- In general terms, CFD modeling results are found to closely match experimental ones in terms of global combustion metrics, such as tip penetration, ignition delay and lift-off length. However, stabilization of lift-off length for  $OME_1$  occurs at shorter distances to the nozzle, and CFD predicts ignition for  $OME_1$  at the lowest ambient temperature, which does not occur in experiments.
- The combination of ambient temperature and different reactivity for both fuels has enabled the transition from a high reactivity typical diffusion flame structure ( $OME_x$  at 1000–900 K) towards lower reactivity cases, where lift-off length may eventually be longer than the length of the stoichiometric surface, and hence the flame stabilizes at very lean conditions, i.e. a type of lean mixing controlled flame is obtained. This is reflected in the spatial distribution of species. For the diffusion-flame topology,  $CH_2O$  is found at rich mixtures and low temperature, starting slightly upstream of the lift-off length location, while  $OH$  mainly occurs around the stoichiometric surface. For the lower reactivity conditions ( $OME_1$  at 900–800 K),  $CH_2O$  is similarly found upstream of the lift-off length location, while  $OH$  is close to the axis at the flame lift-off length, and may also be found at stoichiometric conditions, but only if lift-off length is shorter than the maximum stoichiometric length.
- Laminar flamelet calculations with  $OME_x$ -type fuels show a typical low temperature ignition on the lean mixtures, moving towards a high temperature ignition in the fuel-rich zone, similar

to typical hydrocarbons. However, ignition in CFD configuration seems to occur on the lean side, especially for  $OME_1$  as well as for the low temperature cases. This results from the finite residence time for relevant mixtures in the spray calculations, compared to the infinite one available for the flamelet ones.

- As a general conclusion, these oxygenated fuels can develop very different flames structures compared to conventional hydrocarbons depending on the ambient temperature. The numerical approach followed here, which has been based upon igniting diffusion flamelets, is able to reproduce a lean mixing-controlled flame structure, although for those situations it under-predicts LOL.

#### CRediT authorship contribution statement

**Jesus Benajes:** Conceptualization, Formal analysis, Resources, Project administration. **Jose M. Garcia-Oliver:** Conceptualization, Formal analysis, Investigation, Writing – original draft, Supervision. **Jose M. Pas-tor:** Conceptualization, Formal analysis, Investigation, Writing – review & editing. **Daiana De Leon-Ceriani:** Conceptualization, Formal analysis, Investigation, Data curation, Visualization, Writing – original draft.

#### Declaration of competing interest

The authors declare that they have no known competing financial interests or personal relationships that could have appeared to influence the work reported in this paper.

#### Data availability

Data will be made available on request.

#### Acknowledgment

Funding for open access charge: CRUE-Universitat Politècnica de València.

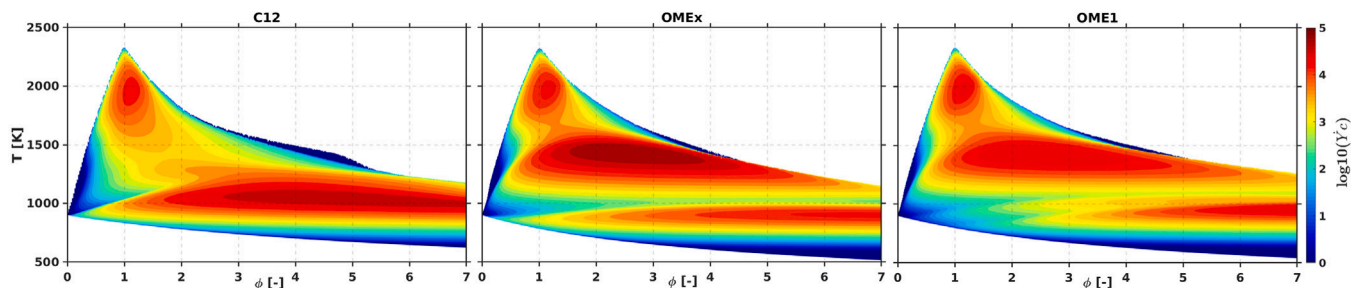


Fig. A.14. Chemical source term  $\dot{Y}_c = dY_c/dt$  for homogeneous reactor calculations in terms of equivalence ratio and temperature.

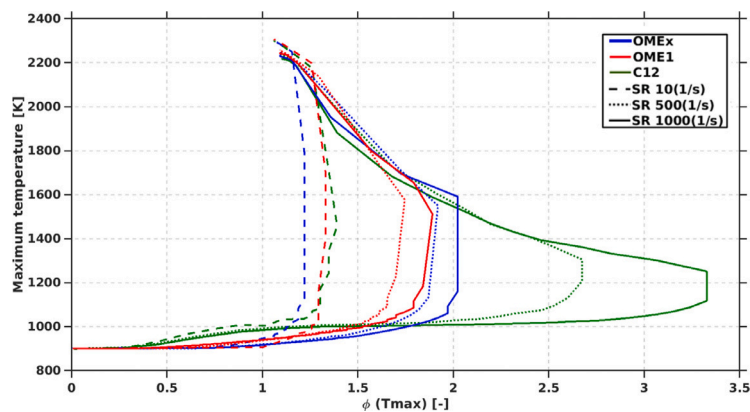


Fig. A.15. Evolution of maximum temperature in the flamelet during autoignition against the equivalence ratio value at which it occurs for OMEx and OME1 at three strain rate values, namely 10, 500 and 1000 (1/s).

## Appendix. Selected plots versus equivalence ratio

Most of the results in the analysis section dealing with flamelets have been plotted against mixture fraction. The purpose of the authors when using the mixture fraction axis was to highlight the important role of mixing on absolute terms, which is crucial in spray combustion. Furthermore, mixture fraction can be more easily compared to axial distance to the nozzle, as shown by the inert spray analysis (Fig. 6). Using equivalence ratio as independent variable is interesting from the chemical point of view, so we have included Figs. A.14 and A.15, which are identical to Figs. 3 and 5 but with equivalence ratio as independent variable.

## References

- [1] Bongartz D, Burre J, Mitsos A. Production of oxymethylene dimethyl ethers from hydrogen and carbon dioxide - part I: Modeling and analysis for OME1. *Ind Eng Chem Res* 2019;58:4881–9.
- [2] Burre J, Bongartz D, Mitsos A. Production of oxymethylene dimethyl ethers from hydrogen and carbon dioxide - part II: Modeling and analysis for OME3-5. *Ind Eng Chem Res* 2019;58:5567–78.
- [3] Siegemund S, Trommler M, Schmidt P, Weindorf W, Zittel W, Raksha T, Zerhusen J. E-fuels study - potential of electricity based fuels for low emission transport in the European Union.
- [4] United Nation climate change: the Paris agreemen. 2020, Available at <https://unfccc.int/process-and-meetings/the-paris-agreement/the-paris-agreement> accessed on 05/02/2020.
- [5] Goeb D, Davidovic M, Cai L, Pancharia P, Bode M, Jacobs S, Beekmann J, Willems W, Heufer KA, Pitsch H. Oxymethylene ether-n-dodecane blend spray combustion: Experimental study and large-eddy simulations. *Proc Combust Inst* 2020;000:1–9.
- [6] Awad OI, Ma X, Kamil M, Ali OM, Ma Y, Shuai S. Science of the total environment overview of polyoxymethylene dimethyl ether additive as an eco-friendly fuel for an internal combustion engine : Current application and environmental impacts. *Sci Total Environ* 2020;715:136849.
- [7] García A, Gil A, Monsalve-Serrano J, Sari RL. OMEx-diesel blends as high reactivity fuel for ultra-low NOx and soot emissions in the dual-mode dual-fuel combustion strategy. *Fuel* 2020;275:117898.
- [8] Pastor JV, García-Oliver JM, Micó C, García-Carrero AA, Gómez A. Experimental study of the effect of hydrotreated vegetable oil and oxymethylene ethers on main spray and combustion characteristics under engine combustion network spray a conditions. *Appl Sci* 2020;10(16):5460.
- [9] Pastor JV, García A, Micó C, Lewiski F. An optical investigation of fischer-tropsch diesel and oxymethylene dimethyl ether impact on combustion process for CI engines. *Appl Energy* 2020;260:114238.
- [10] Pastor JV, Garcia-Oliver JM, Micó C, Tejada FJ. Comparison of the diffusive flame structure for dodecane and OMExFuels for conditions of spray a of the ECN. *SAE Tech Pap* 2020;(2020):1–10.
- [11] Engine combustion network. <https://ecn.sandia.gov/>.
- [12] Omari A, Heuser B, Pischinger S. Potential of oxymethylenether-diesel blends for ultra-low emission engines. *Fuel* 2017;209:232–7.
- [13] Benajes J, García-Oliver J, Pastor J, de León-Ceriani D. A computational study on OME1 spray combustion under ECN Spray A conditions. *Tech. rep., ILASS Asia Paper*; 2020.
- [14] Mira D, Perez-Sanchez E, Surapaneni A, Benajes J, Garcia-Oliver J, Pastor J, De Leon-Ceriani D. LES study on spray combustion with renewable fuels under ECN Spray-A conditions. 2021.
- [15] Cai L, Jacobs S, Langer R, vom Lehn F, Heufer KA, Pitsch H. Auto-ignition of oxymethylene ethers (OMEn, n=2–4) as promising synthetic e-fuels from renewable electricity: shock tube experiments and automatic mechanism generation. *Fuel* 2020;264:116711.
- [16] Desantes JM, García-Oliver JM, Novella R, Pachano L. A numerical study of the effect of nozzle diameter on diesel combustion ignition and flame stabilization. *Int J Engine Res* 2019;21(1):101–21.
- [17] Goodwin DG, Speth RL, Moffat HK, Weber BW. Cantera: An object-oriented software toolkit for chemical kinetics, thermodynamics, and transport processes.
- [18] Naud B, Novella R, Pastor JM, Winklinger JF. RANS modelling of a lifted H2/N2 flame using an unsteady flamelet progress variable approach with presumed PDF. *Combust Flame* 2015;162(4):893–906.
- [19] CONVERGE CFD Software. <https://convergecf.com>.
- [20] Jacobs S, Döntgen M, Alquaity AB, Kopp WA, Kröger LC, Burke U, Pitsch H, Leonhard K, Curran HJ, Heufer KA. Detailed kinetic modeling of dimethoxymethane. Part II: Experimental and theoretical study of the kinetics and reaction mechanism. *Combust Flame* 2019;205:522–33.

- [21] Yao T, Pei Y, Zhong BJ, Som S, Lu T, Luo KH. A compact skeletal mechanism for n-dodecane with optimized semi-global low-temperature chemistry for diesel engine simulations. *Fuel* 2017;191:339–49.
- [22] Peters N. Laminar diffusion flamelet models in non-premixed turbulent combustion. *Prog Energy Combust Sci* 1984;10(3):319–39.
- [23] Pachano L. CFD modeling of combustion and soot production in diesel spray. (PhD), 2020.
- [24] Payri F, Novella R, Pastor J, Pérez-Sánchez E. Evaluation of the approximated diffusion flamelet concept using fuels with different chemical complexity. *Appl Math Model* 2017;49:354–74.
- [25] Desantes J, García-Oliver J, Novella R, Pérez-Sánchez E. Application of an unsteady flamelet model in a RANS framework for spray a simulation. *Appl Therm Eng* 2017;117:50–64.
- [26] García-Oliver JM, Novella R, Pastor JM, Winklinger JF. Evaluation of combustion models based on tabulated chemistry and presumed probability density function approach for diesel spray simulation. *Int J Comput Math* 2014;91(1):14–23.
- [27] Pera C, Colin O, Jay S. Development of a FPI detailed chemistry tabulation methodology for internal combustion engines. *Oil Gas Sci Technol Rev l'IFP* 2009;64:243–58.
- [28] Mastorakos E. Ignition of turbulent non-premixed flames. *Prog Energy Combust Sci* 2009;35(1):57–97.
- [29] Payri F, García-Oliver JM, Novella R, Pérez-Sánchez EJ. Influence of the n-dodecane chemical mechanism on the CFD modelling of the diesel-like ECN spray a flame structure at different ambient conditions. *Combust Flame* 2019;208:198–218.
- [30] Desantes JM, Pastor JV, García-Oliver JM, Briceño FJ. An experimental analysis on the evolution of the transient tip penetration in reacting diesel sprays. *Combust Flame* 2014;161:2137–50.
- [31] Payri R, García-Oliver JM, Xuan T, Bardi M. A study on diesel spray tip penetration and radial expansion under reacting conditions. *Appl Therm Eng* 2015;90:619–29.
- [32] Desantes JM, Pastor JV, García-Oliver JM, Pastor JM. A 1D model for the description of mixing-controlled reacting diesel sprays. *Combust Flame* 2009;156:234–49.
- [33] Desantes JM, García-Oliver JM, Xuan T, Vera-Tudela W. A study on tip penetration velocity and radial expansion of reacting diesel sprays with different fuels. *Fuel* 2017;207:323–35.
- [34] Benajes J, Payri R, Bardi M, Martí-Aldaraví P. Experimental characterization of diesel ignition and lift-off length using a single-hole ECN injector. *Appl Therm Eng* 2013;58:554–63.